

# Layered van der Waals topological metals of TaTMTe<sub>4</sub> (TM = Ir, Rh, Ru) family

G. Shipunov,<sup>1,\*</sup> B.R. Piening,<sup>1</sup> C. Wuttke,<sup>1</sup> T. A. Romanova,<sup>2</sup> A. V. Sadakov,<sup>2</sup>

O. A. Sobolevskiy,<sup>2</sup> E. Yu. Guzovsky,<sup>2</sup> A. S. Usoltsev,<sup>2</sup> V. M. Pudalov,<sup>2</sup>

D. Efremov,<sup>1</sup> S. Subakti,<sup>1</sup> D. Wolf,<sup>1</sup> A. Lubk,<sup>1</sup> B. Büchner,<sup>1,3</sup> and S. Aswartham<sup>1,†</sup>

<sup>1</sup>*Institute for Solid State Research, Leibniz IFW Dresden, Helmholtzstr. 20, 01069 Dresden, Germany*

<sup>2</sup>*P.N. Lebedev Physical Institute, Russian Academy of Sciences, 119991 Moscow, Russia*

<sup>3</sup>*Institute of Solid State and Materials Physics, Technische Universität Dresden, 01062 Dresden, Germany*

(Dated: March 7, 2022)

Layered van der Waals materials of the family TaTMTe<sub>4</sub> (TM=Ir, Rh, Ru) are showing very interesting electronic properties. Here we report the synthesis, crystal growth and structural characterization of TaIrTe<sub>4</sub>, TaRhTe<sub>4</sub>, TaIr<sub>1-x</sub>Rh<sub>x</sub>Te<sub>4</sub> ( $x = 0.06; 0.14; 0.78; 0.92$ ) and Ta<sub>1+x</sub>Ru<sub>1-x</sub>Te<sub>4</sub> single crystals. For Ta<sub>1+x</sub>Ru<sub>1-x</sub>Te<sub>4</sub> off-stoichiometry is shown. X-ray powder diffraction confirms that TaRhTe<sub>4</sub> is isostructural to TaIrTe<sub>4</sub>. We show that all these compounds are metallic with diamagnetic behavior. Ta<sub>1.26(2)</sub>Ru<sub>0.75(2)</sub>Te<sub>4.000(8)</sub> exhibits an upturn in the resistivity at low temperatures which is strongly field dependent. Below  $T \approx 4$  K we observed signatures of the superconductivity in the TaIr<sub>1-x</sub>Rh<sub>x</sub>Te<sub>4</sub> compounds for  $x = 0.92$ . Magnetotransport measurements on all samples show weak magnetoresistance (MR) field dependence that is typically quadratic-in-field. However, for TaIr<sub>1-x</sub>Rh<sub>x</sub>Te<sub>4</sub> with  $x \approx 0.78$ , the MR has a linear term dominating in low fields that indicates the presence of Dirac cones in the vicinity of the Fermi energy. For TaRhTe<sub>4</sub> series the MR is almost isotropic. We have performed electronic structure calculations for isostructural TaIrTe<sub>4</sub> and TaRhTe<sub>4</sub> together with the projected total density of states. The main difference is appearance of the Rh-band close to the Fermi level.

## I. INTRODUCTION

Layered van der Waals two dimensional materials with sizable spin-orbit coupling effects such as WTe<sub>2</sub> and MoTe<sub>2</sub>, have been showing a wide array of fascinating properties, which might be deliberately modified by a variety of parameters, such as composition, thickness, etc [1] makes them even more attractive to gain insight into those physical effects. Recent reports demonstrate type II Weyl semimetallic behavior, both theoretically and experimentally, in both T<sub>d</sub>-MoTe<sub>2</sub> and WTe<sub>2</sub> compound [2–5]. MoTe<sub>2</sub> is also found to host an edge supercurrent [6], to be superconductive [7] with strong en-

hancement of  $T_c$  in point-contact measurements [8] and with sulfur substitution [9] and in monolayers [10]. Moreover, MoTe<sub>2</sub> and WTe<sub>2</sub> exhibit reversible metal-insulator transition, making them attractive candidates for two-dimensional nanoelectronics [11, 12]. WTe<sub>2</sub> shows similar array of properties: the compound is known to host quantum spin Hall state [13], and has large non-saturating magnetoresistance (MR) [14, 15]. Another feature of this structure is the possibility of formation of polar domains. As reported in [16, 17], WTe<sub>2</sub> and MoTe<sub>2</sub> demonstrate switchable spontaneous polarization and a natural ferroelectric domain structure, WTe<sub>2</sub> even at room temperature. Combined with metallic conductivity, this makes those materials first reported real-world examples of a ferroelectric metal materials.

Due to all the fascinating properties the search for materials with similar crystal structure is an active area of research. TaIrTe<sub>4</sub> structure can be derived from WTe<sub>2</sub> by substituting all W atoms with Ta and Ir ordered into zigzag chains along  $a$  direction, where Ir and Ta atoms alternating along the chain (Fig. 1) [18, 19]. TaIrTe<sub>4</sub> has been predicted to host Weyl fermions [20], hosting only four Weyl points (WPs), the minimal number of WPs a WSM with time-reversal invariance can host. Later on signatures of the WPs were found in ARPES [21]. Thickness-related properties were also reported, e.g. in mono- and bilayer TaIrTe<sub>4</sub> quantum hall effect was reported [22], while bulk crystals show room-temperature nonlinear Hall effect with temperature-induced sign change [23]. Moreover TaIrTe<sub>4</sub> is reported to host surface superconductivity with critical temperatures of up to 1.54 K [24]. Among other members of this ternary telluride family NbIrTe<sub>4</sub> was proposed to host type-II Weyl fermions with experimental indica-

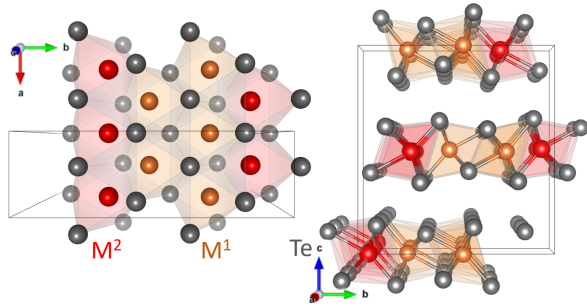


FIG. 1. Schematics of crystal structure of TMTe<sub>2</sub> and TaTMTe<sub>4</sub> compounds.  $M^1=M^2=W$  in case of WTe<sub>2</sub> and  $M^1=TM$ ,  $M^2=Ta$  for TaTMTe<sub>4</sub>. Note the reduced distance between  $M^1$  and  $M^2$  forming a zigzag chains along  $a$ .

\* g.shipunov@ifw-dresden.de

† s.aswartham@ifw-dresden.de

tions in charge transport measurements [25]. This material also demonstrates non-saturating MR [26]. Recently both binary ( $\text{WTe}_2$ ,  $\text{MoTe}_2$ ) and ternary ( $\text{TaTMTe}_4$ ,  $\text{TM}=\text{Ir, Rh, Ru}$ ) tellurides showed bi-stable resistive metal-insulator switching in point contact measurements at room temperature, bringing those materials closer to applications. [12]

Original reports of the  $\text{TaIrTe}_4$  structure also asserts the existence of several other  $\text{MM}^*\text{Te}_4$  compounds and authors furthermore show that among other compounds  $\text{TaRhTe}_4$  and  $\text{TaRuTe}_4$  exist and suggest that  $\text{TaRhTe}_4$  might be isostructural to  $\text{TaIrTe}_4$ , while  $\text{TaRuTe}_4$  might be disordered analogue of the  $\text{TaIrTe}_4$ . [18, 19] This wide array of iso- or similarly structured compounds makes this family a large playground to study the dependence of physical properties on parameters such as lattice size, interatomic distances, outer shell electron number, etc. Beyond initial structural studies of powder samples no further characterization of structural and physical properties on single crystals have been reported. Further chemical and structural investigation of those compounds provides better description of the material at hand, as well as more precise input parameters for theory models.

Here we report crystal growth of 3 members of  $\text{TaTMTe}_4$  family, i.e.  $\text{TaIrTe}_4$ ,  $\text{TaRhTe}_4$  and  $\text{Ta}_{1.26(2)}\text{Ru}_{0.75(2)}\text{Te}_{4.000(8)}$ . Also, we have successfully grown single crystals of doped series such as  $\text{TaIr}_{1-x}\text{Rh}_x\text{Te}_4$ . Further, we discuss composition of acquired samples which is followed by an assessment of the structure of the materials with x-ray and electron diffraction methods. Finally we report results of magnetotransport measurements for selected crystals.

## II. EXPERIMENTAL

### A. crystal growth

Single crystals of  $\text{TaIrTe}_4$ ,  $\text{TaRhTe}_4$ , and  $\text{Ta}_{1+x}\text{Ru}_{1-x}\text{Te}_4$  were grown via self-flux method. Powders of Ta (Alfa Aesar, powder 325 mesh, 99.97%), transition metal,  $\text{TM}=\text{Ir}$  (Alfa Aesar, powder 325 mesh, 99.9%), Rh (Evochem, powder, 99.95%), Ru (MaTecK, powder,  $< 60\mu\text{m}$ , 99.9%) correspondingly, and Te (Alfa Aesar, powder 18 mesh, 99.999%) were mixed in  $\text{Ta:TM:Te}=1:1:20$  molar ratio and thoroughly ground by hand in agate mortar. Afterwards reaction mixture was loaded into Canfield crucible set [27], which in turn was placed in evacuated fused quartz ampule. The mixture was heated up to  $970^\circ\text{C}$  at  $100^\circ\text{C/h}$ , dwelled at this temperature for 24 h, and subsequently slowly cooled at the rate of  $1.5^\circ\text{C/h}$  to final temperature of  $600^\circ\text{C}$ . Further, the crucible was taken out of hot furnace, turned over and instantly put to a centrifuge which facilitated flux removal. Afterwards, crystal surfaces contaminated by small amount of the flux were mechanically cleaved off before further studies. Furthermore, a substitution series of  $\text{TaIr}_{1-x}\text{Rh}_x\text{Te}_4$  was synthesized. For growth

of this substitution series mixture of elemental powders with molar ratio  $\text{Ta:Ir}_{1-x}\text{Rh}_x\text{Te}=1:1:20$  for  $x = 0.1, 0.3, 0.7$  and  $0.9$  was prepared as described for ternary compounds, after which the mixture was heated to  $1000^\circ\text{C}$ , held at this temperature for 24 h, and then cooled over course of 133 h to  $700^\circ\text{C}$ , after which the reaction mixture was centrifuged in aforementioned manner.

### B. characterization

#### 1. composition and structure

The composition of the as grown single crystals was determined by energy-dispersive x-ray spectroscopy (EDX), employing an electron beam probe in a scanning electron microscope (accelerating voltage 30 kV, current 552 pA). Structural characterization and phase purity was confirmed by means of powder X-ray diffraction using a STOE powder diffractometer (Bragg-Brentano transmission geometry,  $2\theta:\omega$  scan,  $\text{Co } K_{\alpha 1}$  or  $\text{Mo } K_{\alpha 1}$  radiation, curved Ge (111) monochromator). Rietveld refinement of the x-ray data was carried out with FullProf [28] and Jana2006 [29] software packages.

Selected area electron diffraction (SAED) on thin exfoliated  $\text{TaTMTe}_4$  ( $\text{TM}=\text{Ir, Ru, Rh}$ ) was utilized by employing FEI Tecnai F20 transmission electron microscope (TEM) with  $\text{LaB}_6$  emitter operated at 200 kV acceleration voltage. The  $\text{TaTMTe}_4$  crystals used in this work were mechanically exfoliated using commercially available adhesive tape (eco, tesa). The exfoliated  $\text{TaTMTe}_4$  crystals were separated from the tape by immersion in 10 mL of acetone and isopropanol (1:1) solution in 12 mL glass sample vial. Ultrasonification (frequency  $\approx 35$  kHz) was employed to assist the separation of  $\text{TaTMTe}_4$ -flakes from the tape surface for two hours ( $8 \times 15$  minutes sonication process with 5 minutes breaks between the 15 minutes session). The micrometer-sized  $\text{TaTMTe}_4$  flakes were then transferred to the TEM lacey-carbon Cu grids using a standard pipette. To ensure the cleanliness of the  $\text{TaTMTe}_4$ -flakes the elemental composition of every  $\text{TaTMTe}_4$ -flake was confirmed by in-situ TEM-EDX before collection of the SAED pattern. Theoretical kinematic electron diffraction patterns were computed and visualized using the SingleCrystal software package version 3.1.5, (CrystalMaker Software Ltd., UK).

#### 2. physical properties

Magnetic susceptibility was measured using a MPMS superconducting quantum interference device (SQUID) magnetometer from Quantum Design. Transport and magnetotransport measurements with  $\text{TaTMTe}_4$  compounds were performed in fields up to 9 T using a PPMS-9 system from Quantum Design, and up to 16 T using

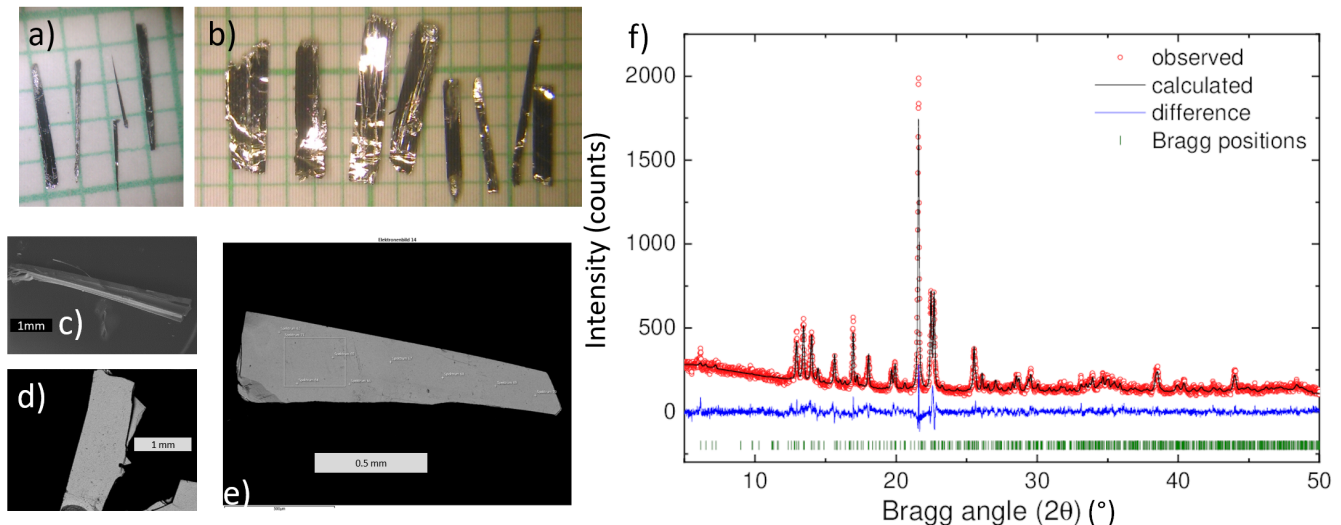


FIG. 2. Images of as-grown  $\text{Ta}_{1.26(2)}\text{Ru}_{0.75(2)}\text{Te}_{4.000(8)}$  (a) and  $\text{TaRhTe}_4$  (b) on a millimeter scale. SEM images of  $\text{TaRhTe}_4$  (c) and  $\text{Ta}_{1.26(2)}\text{Ru}_{0.75(2)}\text{Te}_{4.000(8)}$  (d, e). X-ray powder diffraction plot with the fit by Rietveld method for  $\text{TaRhTe}_4$  ground crystals (f).

CFMS-16 system from Cryogenic respectively. Temperature dependencies of the longitudinal resistivity  $\rho_{xx}$  were measured in the temperature range 2–300 K, and angular dependencies of  $\rho_{xx}(H)$  (the magnetoresistance, MR) at temperatures near 2 K. The data on the type and density of carriers were obtained from Hall effect measurements. Resistivity values were calculated from the measured resistance and the sample dimensions. For the magneto-transport experiment we used the “Hall bar” geometry, where the current was always applied perpendicular to the magnetic field direction.

### III. RESULTS AND DISCUSSION

#### A. composition and structure

The grown crystals depicted on fig. 2 (a, b) are easily cleavable silvery flat needles of up to 0.5 cm in length and up to 0.1 cm in diameter with mass on the order of tens of milligrams. Crystals of  $\text{TaIrTe}_4$  show a needle-like appearance, while  $\text{TaRhTe}_4$  and  $\text{Ta}_{1.26(2)}\text{Ru}_{0.75(2)}\text{Te}_{4.000(8)}$  are more flattened, in a shape of thin stripes. As-grown crystals are extremely ductile and cleavable, even under regular handling operations. The results of the EDX confirm the nominal stoichiometry for  $\text{TaRhTe}_4$  and  $\text{TaIrTe}_4$  samples. Backscattered-electron SEM images (fig. 2 (c–e)) show uniform intensity, which is indicative of the absence of macroscopic inhomogeneities. Interestingly, the nominal ratio  $\text{Ru}:\text{Ta}=1:1$  as-grown crystals in fact show  $\text{Ta}_{1.26(2)}\text{Ru}_{0.75(2)}\text{Te}_{4.000(8)}$  composition. This  $\text{Ru}:\text{Ta}$  ratio is consistent across different measurement points and different crystals, on natural and freshly cleaved surfaces, with a low EDX statistical error. Assuming the same

connectivity in the structure as in  $\text{TaIrTe}_4$  compound, this composition shift must manifest as structural modification hinted in [18]. This composition shift might be explained by the fact that Ru and Ta radii are quite close, resulting in e.g. mixing of the atoms in the same crystallographic position.

Results of EDX measurements on the  $\text{TaIr}_{1-x}\text{Rh}_x\text{Te}_4$  are presented in table I. We see Rh/Ir substitution, with composition consistently shifted towards metal with the higher concentration.

For characterization of the structure powder x-ray diffraction (PXRD) was carried out including further analysis by Rietveld method. Results of the x-ray powder diffraction on  $\text{TaRhTe}_4$  powdered crystals are presented in fig. 2 (f); PXRD patterns for  $\text{Ta}_{1.26(2)}\text{Ru}_{0.75(2)}\text{Te}_{4.000(8)}$  and  $\text{TaIr}_{1-x}\text{Rh}_x\text{Te}_4$  are presented on fig. 10 in appendix, due to strong texture in both cases and high ductility in case of  $\text{Ta}_{1.26(2)}\text{Ru}_{0.75(2)}\text{Te}_{4.000(8)}$  Rietveld analysis of those didn’t prove to be feasible. One observes fig. 2 diffraction shows broad reflections, which can be attributed to high ductility and ease of cleavage of the material.  $\text{TaIrTe}_4$  was refined in the structural model presented in ICSD [18], (ICSD №73322, space group  $Pmn2_1$ ). As reported by Mar et al. [18], we see that in case of  $\text{TaRhTe}_4$  compound diffraction pattern is quite similar to  $\text{TaIrTe}_4$ . The  $\text{TaRhTe}_4$  diffraction pattern was clearly indexed in  $Pmn2_1$  space group, so for further Rietveld analysis we selected  $\text{TaIrTe}_4$  as initial structure model, with Ir positions substituted by Rh with approximate lattice parameters extracted in the indexing step. Refinement in this model yielded lattice parameters of  $a = 3.75670(11)$ ,  $b = 12.5476(5)$ ,  $c = 13.166(3)$  and cell volume of  $V = 620.20(15)$  for  $\text{TaRhTe}_4$ . We observe small change of  $a$

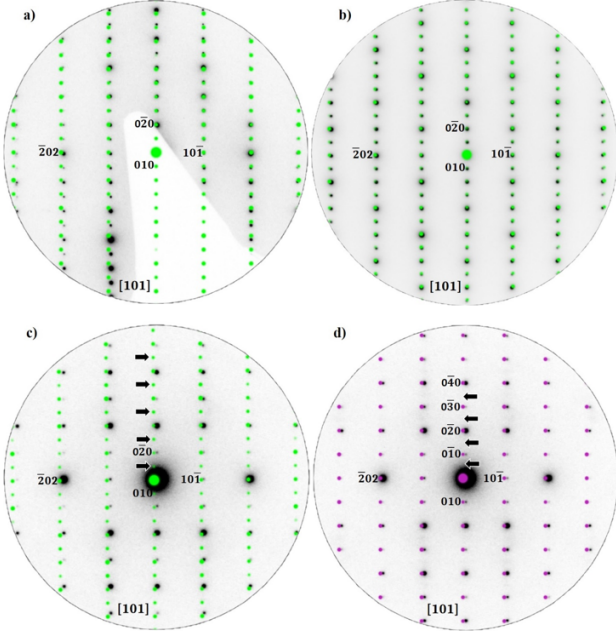


FIG. 3. Selected area electron diffraction (SAED) on TaIrTe<sub>4</sub>, TaRhTe<sub>4</sub> and Ta<sub>1.26(2)</sub>Ru<sub>0.75(2)</sub>Te<sub>4.000(8)</sub>. (a,b) SAED patterns of representative TaIrTe<sub>4</sub> and TaRhTe<sub>4</sub> nanoflake oriented along [101] zone axis overlaid with theoretical SAED patterns (green dots) using  $Pmn2_1$  (N31) space group obtained from PXRD data refinement results in this work. (c,d) SAED pattern of a representative Ta<sub>1.26(2)</sub>Ru<sub>0.75(2)</sub>Te<sub>4.000(8)</sub> nanoflake oriented along [101] zone axis overlaid with theoretical SAED patterns (green dots) using  $Pmn2_1$  (N31) structure derived from TaIrTe<sub>4</sub> (c) and a  $Pmn2_1$  structure derived from WTe<sub>2</sub> (unit cell is halved along  $b$  compared to TaIrTe<sub>4</sub>, d). The simulated reflections are intentionally slightly shifted for better overview. The arrows on the (c) and (d) images are given to mark the different fit between the two crystal models for Ta<sub>1.26(2)</sub>Ru<sub>0.75(2)</sub>Te<sub>4.000(8)</sub>.

and  $c$  parameters  $\Delta a \approx -0.03\text{\AA}$ ;  $\Delta c \approx -0.03\text{\AA}$ , and a considerable increase of  $b$  ( $\Delta b \approx 0.12\text{\AA}$ ) compared to the TaIrTe<sub>4</sub> structure. This can be explained by the smaller radius of the Rh atom, and as a result, might be indicative of tighter, and more extended zigzag chains in the structure. Refined atomic positions are presented in table II. With that we can conclude that the TaRhTe<sub>4</sub> compound is isostructural to TaIrTe<sub>4</sub>, which provides the opportunity to study change of physical properties with the change of lattice parameters and isovalent substitution.

SAED on individual TaTMTe<sub>4</sub> nanoflakes exfoliated from single crystals was performed to elaborate the crystallographic information obtained from the PXRD data reported in this work (Fig. 3). The SAED patterns for TaTMTe<sub>4</sub> acquired in [101] orientation are compared with simulated electron diffraction (ED) pattern using  $Pmn2_1$  (N31) space group. Here the [101] zone axis allows to distinguish lattice modulations in ternary TaTMTe<sub>4</sub> systems along  $b$ -direction in reciprocal space.

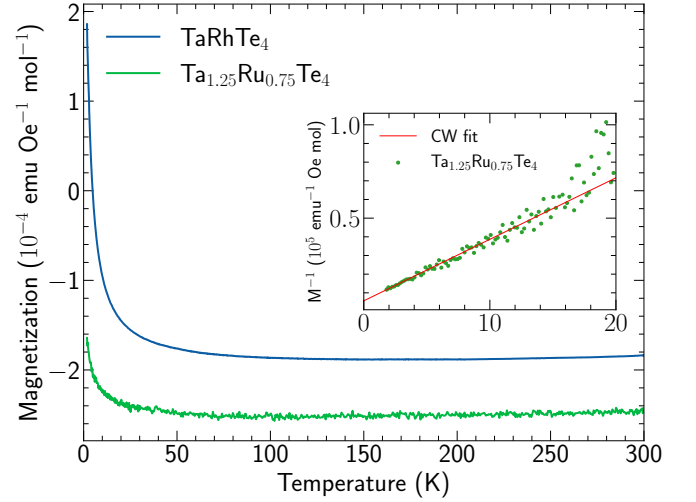


FIG. 4. Temperature dependence of molar magnetization for TaRhTe<sub>4</sub> and Ta<sub>1.26(2)</sub>Ru<sub>0.75(2)</sub>Te<sub>4.000(8)</sub>; Inset: Curie-Weiss fit of paramagnetic contribution to Ta<sub>1.26(2)</sub>Ru<sub>0.75(2)</sub>Te<sub>4.000(8)</sub> magnetization.

The good agreement of all symmetrical equivalent reflections in the ED patterns for TaIrTe<sub>4</sub> and TaRhTe<sub>4</sub> strongly suggest that these two crystals are isostructural and crystallize in  $Pmn2_1$  space group as described in [18]. Interestingly, the Ta<sub>1.26(2)</sub>Ru<sub>0.75(2)</sub>Te<sub>4.000(8)</sub> electron diffraction patterns show that the unit cell of this compound is halved along  $b$  compared to TaIrTe<sub>4</sub>. To obtain a better fit with the SAED pattern we therefore used a crystal structure for Ta<sub>1.26(2)</sub>Ru<sub>0.75(2)</sub>Te<sub>4.000(8)</sub>, which was derived from WTe<sub>2</sub> phase by filling the two W 2a Wyckoff sites with Ta and Ru respectively. The proposed new structure matches nicely to the experimental SAED data of Ta<sub>1.26(2)</sub>Ru<sub>0.75(2)</sub>Te<sub>4.000(8)</sub> compound (purple dots, Fig. 3 d) and hence also provides a hint concerning the anomaly related to weak  $k = 2n + 1$  reflections reported in [18]. Note, however, that this new structure does not reflect the large off-stoichiometry and the atomic positions and exact symmetry remain unclear as of now. Further studies are therefore required to fully resolve the Ta<sub>1.26(2)</sub>Ru<sub>0.75(2)</sub>Te<sub>4.000(8)</sub> structure.

## B. physical properties

### 1. Magnetization

For ternary compounds the temperature dependence of magnetization was measured. The derived temperature dependence of molar magnetization for TaRhTe<sub>4</sub> and Ta<sub>1.26(2)</sub>Ru<sub>0.75(2)</sub>Te<sub>4.000(8)</sub> is presented in fig. 4. All compounds exhibit diamagnetic behavior, with Curie-Weiss tails at low temperatures. Inset in Fig. 4 shows the Curie-Weiss analysis for Ta<sub>1.26(2)</sub>Ru<sub>0.75(2)</sub>Te<sub>4.000(8)</sub> at temperatures below 20 K. Data confirms absence of any long range magnetic order down to 1.8 K.



### 3. Electronic structure calculations

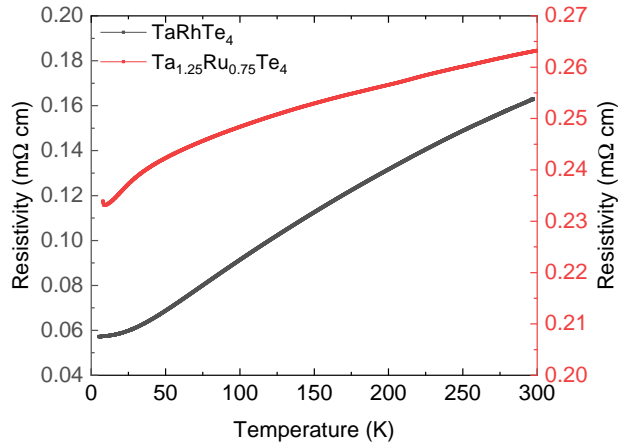


FIG. 5. Temperature dependence of the resistivity for  $\text{Ta}_{1.26(2)}\text{Ru}_{0.75(2)}\text{Te}_{4.000(8)}$  and  $\text{TaRhTe}_4$ .

### 2. Transport and magnetotransport

For stoichiometric  $\text{TaRhTe}_4$  (Fig. 5) as well as for Ir-doped  $\text{TaRh}_{1-x}\text{Ir}_x\text{Te}_4$  compound with  $x = 0.08$  (Fig. 9) the temperature dependency of the diagonal resistivity in zero field flatten below  $\approx 20$  K. In magnetic field, both for  $B \parallel b$  and  $B \parallel c$  (see Fig. 6), the resistivity also follows a classical almost isotropic quadratic dependence. The bulk carrier density determined from Hall resistance measurements (inset to fig. 6  $n \approx 1.7 \times 10^{20} \text{ cm}^{-3}$  for the stoichiometric  $\text{TaRhTe}_4$  is by a factor of two lower compared to well investigated member of the family  $\text{TaIrTe}_4$ . As shown in Fig. 6, the resistivity of  $\text{TaIrTe}_4$  varies quadratically with field which is quite similar in our case of  $\text{TaRhTe}_4$ .  $\text{TaIrTe}_4$  resistivity exhibits a minor (8% at  $B = 9$  T) anisotropy. The Hall resistivity  $\rho_{xy}$  is negative and linearly grows with field, thus indicating dominant  $n$ -type electronic states with a similar bulk carrier density of  $1.8 \times 10^{20} \text{ cm}^{-2}$ . The initial minor anisotropy of the magnetoresistance becomes even lower upon doping with Rh or Ru.

$\text{Ta}_{1.26(2)}\text{Ru}_{0.75(2)}\text{Te}_{4.000(8)}$  demonstrate metallic-type transport behavior (Fig. 5) at least down to 10 K. Although the resistivity shows a markedly different behavior at low temperatures, where it exhibits a minimum at  $T \approx 9$  K, which appears to be a kink followed by a steep upturn while further lowering the temperature below 9 K. The origin of such non-monotonic resistivity remains unclear and requires further investigation.

The 22% substitution of Rh by Ir does not change significantly the resistivity  $T$ -dependence: RRR remains almost unchanged, whereas the carrier density increases by 34% to  $2.3 \times 10^{20} \text{ cm}^{-3}$ , and the magnetoresistance becomes fully isotropic. Interestingly, for the intermediate Ir-doping of 8%, the sample shows signatures of the emerging superconducting (SC) transition (see Fig. 9 in Appendix).

We have performed calculations on the electronic structure within the DFT theory. The full relativistic generalized gradient approximation (GGA) in the Perdew-Burke-Ernzerhof variant is used for the exchange correlation potential implemented in the full potential local orbital band-structure package (FPLO) [30, 31]. For the Brillouin zone (BZ) integration we used the tetrahedron method with  $12 \times 12 \times 12 k$ -mesh. The obtained electronic density of states (DOS) is presented in Fig. 7 decreases slightly at the Fermi level and then increases continuously similar  $\text{TaIrTe}_4$ . Band structures of  $\text{TaRhTe}_4$  with  $\text{TaIrTe}_4$  are presented in Fig. 8. The main difference is appearance of the Rh-band close to the Fermi level. A detailed look at electronic structure properties of  $\text{TaRhTe}_4$  together with investigation via ARPES will be reported elsewhere [32]. The orbital contribution to the electronic band structure is given in the Fig. 8. The rest of the bands are similar for both structures. It explains the similarity in the physical properties of both materials.

## IV. CONCLUSION

In conclusion, we reported single crystal growth of layered van der Waals materials of the family  $\text{TaTMTe}_4$  (TM=Ir,Rh,Ru), as well as several  $\text{TaIr}_{1-x}\text{Rh}_x\text{Te}_4$  compounds. We confirmed the nominal compositions via SEM-EDX. In the  $\text{Ta}_{1+x}\text{Ru}_{1-x}\text{Te}_4$  case we demonstrate that the compound is not stoichiometric with an actual composition of  $\text{Ta}_{1.26(2)}\text{Ru}_{0.75(2)}\text{Te}_{4.000(8)}$ . X-ray powder diffraction and further Rietveld refinement confirms that  $\text{TaRhTe}_4$  is isostructural to  $\text{TaIrTe}_4$  and crystallizes in non-centrosymmetric orthorhombic  $Pmn2_1$  space group with a similar connectivity as  $\text{WTe}_2$ . SAED results indicate that  $\text{Ta}_{1.26(2)}\text{Ru}_{0.75(2)}\text{Te}_{4.000(8)}$  is a disordered analog of  $\text{TaIrTe}_4$  structure type and further investigation of the structure is needed. Substitution series of  $\text{TaIr}_{1-x}\text{Rh}_x\text{Te}_4$  were obtained for  $x = 0.06; 0.14, 0.78, 0.92$  and we investigated magnetic and magnetotransport properties of the grown single crystals.

All samples have electronic ( $n$ -type) conduction. Any substitution of Rh or Ir was found to reduce mobility. All samples show weak MR field dependence. For the Rh series the MR is almost isotropic. Some compounds show a linear MR in low fields, atop of the parabolic one.  $\text{Ta}_{1.26(2)}\text{Ru}_{0.75(2)}\text{Te}_{4.000(8)}$  shows parabolic magnetoresistance which flattens out in high fields at the temperatures above 9 K. Magnetoresistance measurements below 9 K show a clear anomaly in fields below 5 T. We have performed electronic structure calculations using DFT for isostructural  $\text{TaIrTe}_4$  and  $\text{TaRhTe}_4$  together with the projected total density of states. The main difference is appearance of the Rh-band close to the Fermi level.

Due to the topological properties of the electronic band structure, the recent observation of the resistive switch-

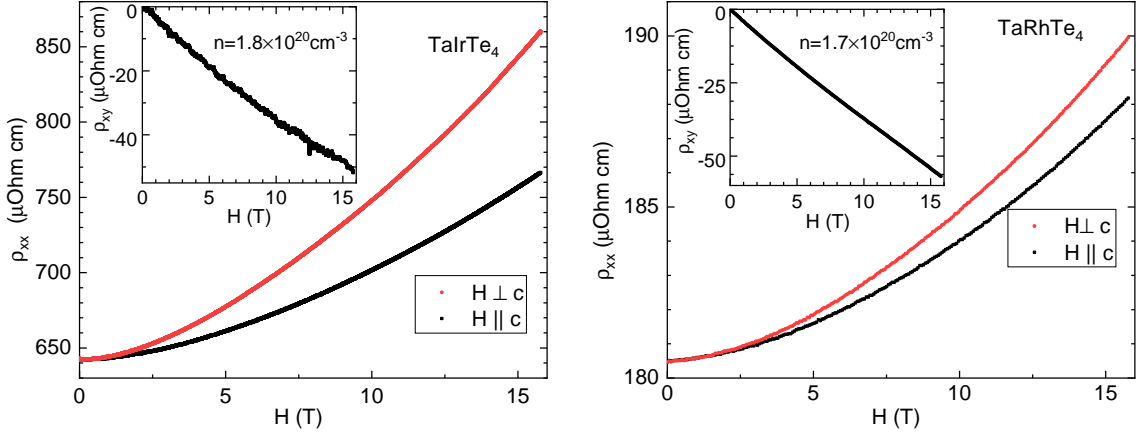


FIG. 6. Left panel: magnetic field dependence of the diagonal resistivity  $\rho_{xx}$  for TaIrTe<sub>4</sub> at two field orientations. Inset: Hall resistivity  $\rho_{xy}$  versus magnetic field. Temperature  $T = 2$  K. Right panel: magnetic field dependence of  $\rho_{xx}$  for TaRhTe<sub>4</sub> at two field orientations. Inset:  $\rho_{xy}$  versus magnetic field.  $T = 2$  K.  $n = 1.7 \times 10^{20} \text{ cm}^{-2}$ , as determined from Hall resistivity.

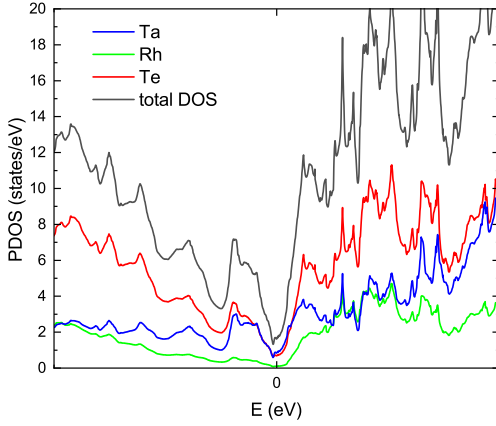


FIG. 7. Total DOS of TaRhTe<sub>4</sub> and the partial contribution of Ta, Rh and Te orbitals.

ing at the room temperature, together with the observed signatures of the superconducting transition, these systems are very interesting for further investigation.

**Acknowledgments** SA acknowledges financial support of Deutsche Forschungsgemeinschaft (DFG) through Grant №AS 523/4-1. SA, DE, BB acknowledge DFG financial support through DFG-RSF project №449494427. BB acknowledges financial support from the projects of the Collaborative Research Center SFB 1143 at the TU Dresden (project-id 247310070) and Würzburg-Dresden Cluster of Excellence on Complexity and Topology in Quantum Matter ct.qmat (EXC 2147, project-id 390858490). AVS, ASU and VMP acknowledge support from RFBR (project # 21-52-12043). SS, DW and AL acknowledge funding from DFG SFB 1415, Project ID №417590517. Transport and magnetotransport measure-

ments were done using equipment of the LPI Shared Facility Center. We acknowledge U. Nitzsche for technical assistance.

**Author contribution** Single crystal growth and characterization experiments, magnetization measurements were performed by GS, BRP, BB and SA. The resistivity and magnetoresistance measurements on Ta<sub>1.26(2)</sub>Ru<sub>0.75(2)</sub>Te<sub>4.000(8)</sub> were performed and analyzed by CW. Resistivity and magnetoresistance measurements were performed and analyzed by TAR, AVS, OAS, EYuG, ASU and VMP. Selected area electron diffraction experiments were performed and interpreted by SS, DW and AL. Electronic band structure calculations were performed by DE. GS and SA wrote the manuscript with input from all co-authors.

**Data availability** The datasets generated during and/or analyzed during the current study are available from the corresponding authors on reasonable request.

**Competing interests** The authors declare no competing financial or non-financial interest.

## V. APPENDIX

We observed an indication of emerging superconductivity (SC) with critical temperature  $T_c = 4$  K in TaRh<sub>1-x</sub>Ir<sub>x</sub>Te<sub>4</sub> compound for  $x = 0.08$  and in TaIr<sub>1-x</sub>Ru<sub>x</sub>Te<sub>4</sub> for  $x = 0.22$ . As an example, we show in Fig. 9 the data for the former compound.

The inset in Fig. 9 zooms in a sharp drop of  $\rho_{xx}(T)$  by  $4 \mu\text{ Ohm}\cdot\text{cm}$  both in zero field as temperature decreases below  $T \approx 4$  K, and at  $T = 2$  K as magnetic field decreases below 0.1 T. These features suggest that the drop of  $\rho_{xx}$  is related with the SC transition at  $T_c \approx 4$  K in zero field. Indeed, the transition temperature shifts to lower values as magnetic field increases, and the critical magnetic field decreases as temperature raises.

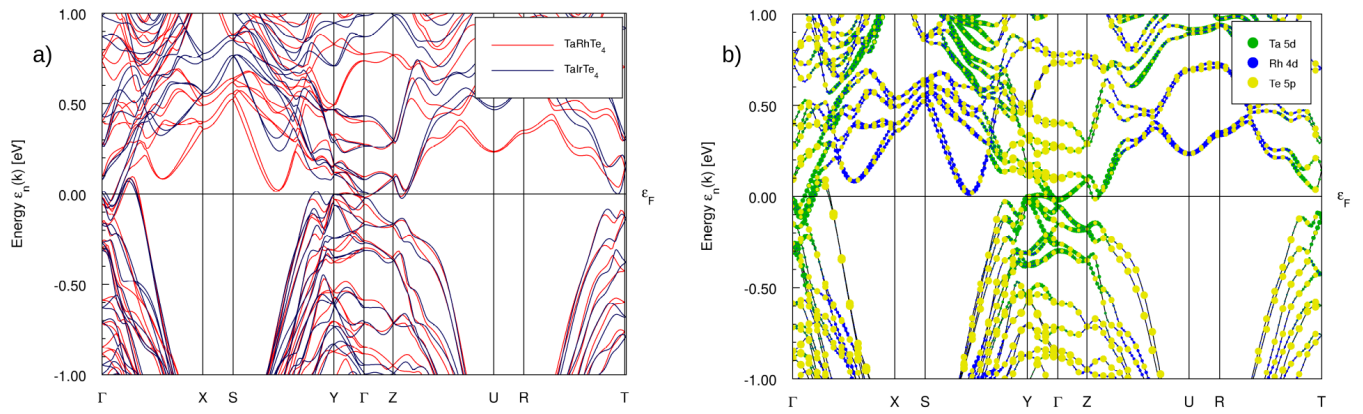


FIG. 8. Band structure TaRhTe<sub>4</sub> vs TaIrTe<sub>4</sub> (a). Orbital contribution to the electronic band structure of TaRhTe<sub>4</sub> (b).

The zero-resistance state is not achieved, apparently because of a very small fraction of the superconducting state. In strong magnetic field, MR shows weak classical quadratic dependence, almost isotropic in  $\theta$ . These slightly doped TaRh<sub>1-x</sub>Ir<sub>x</sub>Te<sub>4</sub> and TaIr(Ru)Te<sub>4</sub> samples,

most likely, contain minor inclusions of several SC phases which emerge in a narrow interval of doping on the compound phase diagram. The interesting issue of potential superconductivity in these compounds requires additional more detailed studies.

- 
- [1] S. Manzheli, D. Ovchinnikov, D. Pasquier, O. V. Yazyev, and A. Kis, 2D transition metal dichalcogenides, *Nature Reviews Materials* **2**, 1 (2017).
  - [2] A. Liang, J. Huang, S. Nie, Y. Ding, Q. Gao, C. Hu, S. He, Y. Zhang, C. Wang, B. Shen, J. Liu, P. Ai, L. Yu, X. Sun, W. Zhao, S. Lv, D. Liu, C. Li, Y. Zhang, Y. Hu, Y. Xu, L. Zhao, G. Liu, Z. Mao, X. Jia, F. Zhang, S. Zhang, F. Yang, Z. Wang, Q. Peng, H. Weng, X. Dai, Z. Fang, Z. Xu, C. Chen, and X. J. Zhou, Electronic Evidence for Type II Weyl Semimetal State in MoTe<sub>2</sub>, arXiv:1604.01706 [cond-mat] (2016).
  - [3] I. Belopolski, S.-Y. Xu, Y. Ishida, X. Pan, P. Yu, D. S. Sanchez, H. Zheng, M. Neupane, N. Alidoust, G. Chang, T.-R. Chang, Y. Wu, G. Bian, S.-M. Huang, C.-C. Lee, D. Mou, L. Huang, Y. Song, B. Wang, G. Wang, Y.-W. Yeh, N. Yao, J. E. Rault, P. Le Fèvre, F. Bertran, H.-T. Jeng, T. Kondo, A. Kaminski, H. Lin, Z. Liu, F. Song, S. Shin, and M. Z. Hasan, Fermi arc electronic structure and Chern numbers in the type-II Weyl semimetal candidate Mo<sub>x</sub>W<sub>1-x</sub>Te<sub>2</sub>, *Physical Review B* **94**, 085127 (2016).
  - [4] L. Huang, T. M. McCormick, M. Ochi, Z. Zhao, M.-T. Suzuki, R. Arita, Y. Wu, D. Mou, H. Cao, J. Yan, N. Trivedi, and A. Kaminski, Spectroscopic evidence for a type II Weyl semimetallic state in MoTe<sub>2</sub>, *Nature Materials* **15**, 1155 (2016).
  - [5] Y. Wu, D. Mou, N. H. Jo, K. Sun, L. Huang, S. L. Bud'ko, P. C. Canfield, and A. Kaminski, Observation of Fermi arcs in the type-II Weyl semimetal candidate WTe<sub>2</sub>, *Physical Review B* **94**, 121113 (2016).
  - [6] W. Wang, S. Kim, M. Liu, F. A. Cevallos, R. J. Cava, and N. P. Ong, Evidence for an edge supercurrent in the Weyl superconductor MoTe<sub>2</sub>, *Science* **368**, 534 (2020).
  - [7] Y. Qi, P. G. Naumov, M. N. Ali, C. R. Rajamathi, W. Schnelle, O. Barkalov, M. Hanfland, S.-C. Wu, C. Shekhar, Y. Sun, V. Süß, M. Schmidt, U. Schwarz, E. Pippel, P. Werner, R. Hillebrand, T. Förster, E. Kampert, S. Parkin, R. J. Cava, C. Felser, B. Yan, and S. A. Medvedev, Superconductivity in Weyl semimetal candidate MoTe<sub>2</sub>, *Nature Communications* **7**, 11038 (2016).
  - [8] Y. Naidyuk, O. Kvitnitskaya, D. Bashlakov, S. Aswartham, I. Morozov, I. Chernyavskii, G. Fuchs, S.-L. Drechsler, R. Hühne, K. Nielsch, B. Büchner, and D. Efremov, Surface superconductivity in the Weyl semimetal MoTe<sub>2</sub> detected by point contact spectroscopy, *2D Materials* **5**, 045014 (2018).
  - [9] F. C. Chen, X. Luo, R. C. Xiao, W. J. Lu, B. Zhang, H. X. Yang, J. Q. Li, Q. L. Pei, D. F. Shao, R. R. Zhang, L. S. Ling, C. Y. Xi, W. H. Song, and Y. P. Sun, Superconductivity enhancement in the S-doped Weyl semimetal candidate MoTe<sub>2</sub>, *Applied Physics Letters* **108**, 162601 (2016).
  - [10] D. A. Rhodes, A. Jindal, N. F. Q. Yuan, Y. Jung, A. Antony, H. Wang, B. Kim, Y.-c. Chiu, T. Taniguchi, K. Watanabe, K. Barmak, L. Balicas, C. R. Dean, X. Qian, L. Fu, A. N. Pasupathy, and J. Hone, Enhanced superconductivity in monolayer td-mote2, *Nano Letters* **21**, 2505 (2021), pMID: 33689385, <https://doi.org/10.1021/acs.nanolett.0c04935>.
  - [11] C. Zhang, S. KC, Y. Nie, C. Liang, W. G. Vandenberghe, R. C. Longo, Y. Zheng, F. Kong, S. Hong, R. M. Wallace, and K. Cho, Charge Mediated Reversible Metal-Insulator Transition in Monolayer MoTe<sub>2</sub> and W<sub>x</sub>Mo<sub>1-x</sub>Te<sub>2</sub> Alloy, *ACS Nano* **10**, 7370 (2016).
  - [12] Y. G. Naidyuk, D. L. Bashlakov, O. E. Kvitnitskaya, B. R. Piening, G. Shipunov, D. V. Efremov, S. Aswartham, and B. Büchner, Switchable topological domains in point contacts based on transition metal tel-

- lurides, arXiv:2011.01569 [cond-mat] (2020).
- [13] S. Tang, C. Zhang, D. Wong, Z. Pedramrazi, H.-Z. Tsai, C. Jia, B. Moritz, M. Claassen, H. Ryu, S. Kahn, J. Jiang, H. Yan, M. Hashimoto, D. Lu, R. G. Moore, C.-C. Hwang, C. Hwang, Z. Hussain, Y. Chen, M. M. Ugeda, Z. Liu, X. Xie, T. P. Devereaux, M. F. Crommie, S.-K. Mo, and Z.-X. Shen, Quantum spin Hall state in monolayer 1T'-WTe<sub>2</sub>, *Nature Physics* **13**, 683 (2017).
  - [14] M. N. Ali, J. Xiong, S. Flynn, J. Tao, Q. D. Gibson, L. M. Schoop, T. Liang, N. Haldolaarachchige, M. Hirschberger, N. P. Ong, and R. J. Cava, Large, non-saturating magnetoresistance in WTe<sub>2</sub>, *Nature* **514**, 205 (2014).
  - [15] L. R. Thoutam, Y. L. Wang, Z. L. Xiao, S. Das, A. Luican-Mayer, R. Divan, G. W. Crabtree, and W. K. Kwok, Temperature-Dependent Three-Dimensional Anisotropy of the Magnetoresistance WTe<sub>2</sub>, *Physical Review Letters* **115**, 046602 (2015).
  - [16] P. Sharma, F.-X. Xiang, D.-F. Shao, D. Zhang, E. Y. Tsybal, A. R. Hamilton, and J. Seidel, A room-temperature ferroelectric semimetal, *Science Advances* **5**, eaax5080 (2019).
  - [17] F.-T. Huang, S. Joon Lim, S. Singh, J. Kim, L. Zhang, J.-W. Kim, M.-W. Chu, K. M. Rabe, D. Vanderbilt, and S.-W. Cheong, Polar and phase domain walls with conducting interfacial states in a Weyl semimetal MoTe<sub>2</sub>, *Nature Communications* **10**, 4211 (2019).
  - [18] A. Mar, S. Jobic, and J. A. Ibers, Metal-metal vs tellurium-tellurium bonding in WTe<sub>2</sub> and its ternary variants TaIrTe<sub>4</sub> and NbIrTe<sub>4</sub>, *Journal of the American Chemical Society* **114**, 8963 (1992).
  - [19] A. Mar and J. A. Ibers, Synthesis and physical properties of the new layered ternary tellurides M<sub>2</sub>IrTe<sub>4</sub> (M = Nb, Ta), and the structure of NbIrTe<sub>4</sub>, *Journal of Solid State Chemistry* **97**, 366 (1992).
  - [20] K. Koepnik, D. Kasinathan, D. V. Efremov, S. Khim, S. Borisenko, B. Büchner, and J. van den Brink, TaIrTe<sub>4</sub>: A ternary type-II Weyl semimetal, *Physical Review B* **93**, 201101 (2016).
  - [21] E. Haubold, K. Koepnik, D. Efremov, S. Khim, A. Fedorov, Y. Kushnirenko, J. van den Brink, S. Wurmehl, B. Büchner, T. K. Kim, M. Hoesch, K. Sumida, K. Taguchi, T. Yoshikawa, A. Kimura, T. Okuda, and S. V. Borisenko, Experimental realization of type-II Weyl state in noncentrosymmetric TaIrTe<sub>4</sub>, *Physical Review B* **95**, 241108 (2017).
  - [22] P.-J. Guo, X.-Q. Lu, W. Ji, K. Liu, and Z.-Y. Lu, Quantum spin Hall effect in monolayer and bilayer TaIrTe<sub>4</sub>, *Physical Review B* **102**, 041109 (2020).
  - [23] D. Kumar, C.-H. Hsu, R. Sharma, T.-R. Chang, P. Yu, J. Wang, G. Eda, G. Liang, and H. Yang, Room temperature nonlinear Hall effect and wireless RF rectification in Weyl semimetal TaIrTe<sub>4</sub>, arXiv:2012.14104 [cond-mat] (2020).
  - [24] Y. Xing, Z. Shao, J. Ge, J. Luo, J. Wang, Z. Zhu, J. Liu, Y. Wang, Z. Zhao, J. Yan, D. Mandrus, B. Yan, X.-J. Liu, M. Pan, and J. Wang, Surface superconductivity in the type II Weyl semimetal TaIrTe<sub>4</sub>, *National Science Review* **7**, 579 (2020).
  - [25] R. Schönemann, Y.-C. Chiu, W. Zheng, V. L. Quito, S. Sur, G. T. McCandless, J. Y. Chan, and L. Balicas, Bulk Fermi surface of the Weyl type-II semimetallic candidate NbIrTe<sub>4</sub>, *Physical Review B* **99**, 195128 (2019).
  - [26] W. Zhou, B. Li, C. Q. Xu, M. R. van Delft, Y. G. Chen, X. C. Fan, B. Qian, N. E. Hussey, and X. Xu, Nonsaturating Magnetoresistance and Nontrivial Band Topology of Type-II Weyl Semimetal NbIrTe<sub>4</sub>, *Advanced Electronic Materials* **5**, 1900250 (2019).
  - [27] P. C. Canfield, T. Kong, U. S. Kaluarachchi, and N. H. Jo, Use of frit-disc crucibles for routine and exploratory solution growth of single crystalline samples, *Philosophical Magazine* **96**, 84 (2016).
  - [28] J. Rodríguez-Carvajal, Recent advances in magnetic structure determination by neutron powder diffraction, *Physica B: Condensed Matter* **192**, 55 (1993).
  - [29] V. Petříček, M. Dušek, and L. Palatinus, Crystallographic computing system JANA2006: General features, *Zeitschrift für Kristallographie - Crystalline Materials* **229** (2014).
  - [30] FPLO, <https://www.fplo.de/>.
  - [31] K. Koepnik and H. Eschrig, Full-potential nonorthogonal local-orbital minimum-basis band-structure scheme, *Phys. Rev. B* **59**, 1743 (1999).
  - [32] B. Sadhukhan, E. Haubold, G. Shipunov, A. Fedorov, S. Aswartham, M. Richter, S. V. Borisenko, J. van den Brink, and R. Ray, Topological electronic properties of the ternary weyl semimetal TaRhTe<sub>4</sub> (2021), in preparation.



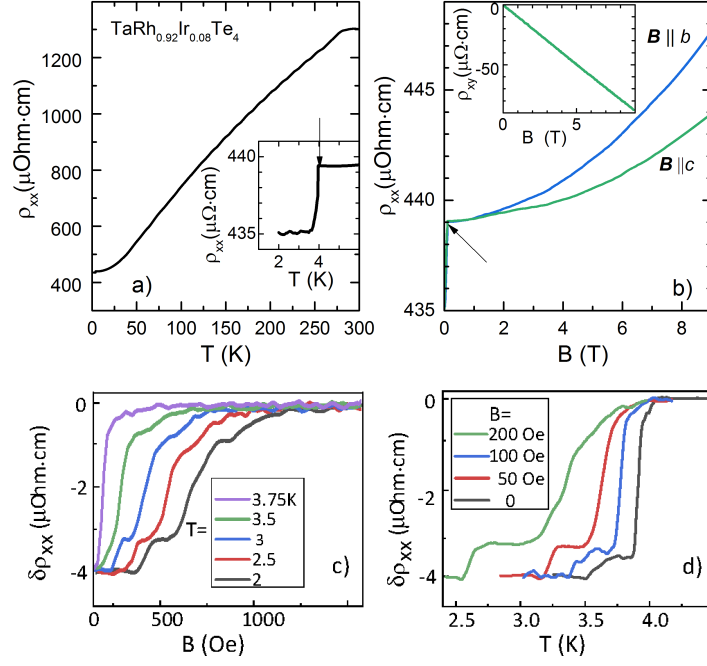


FIG. 9. (a) Temperature dependence of  $\rho_{xx}$  for  $\text{TaRh}_{0.92}\text{Ir}_{0.08}\text{Te}_4$ . Inset shows low temperature region of  $\rho_{xx}(T)$ . (b)  $\rho_{xx}$  versus magnetic field at two field orientations, measured at  $T = 2\text{ K}$ . Inset: magnetic field dependence of the Hall resistivity  $\rho_{xy}$ . Arrows on panels (a) and (b) point at the onset of the SC transition; (c) low-field region of the  $\rho_{xx}(H)$  dependencies measured at several fixed temperatures. (d) low-temperature region of the  $\rho_{xx}(T)$  dependencies measured at several field values at  $T = 2\text{ K}$ .

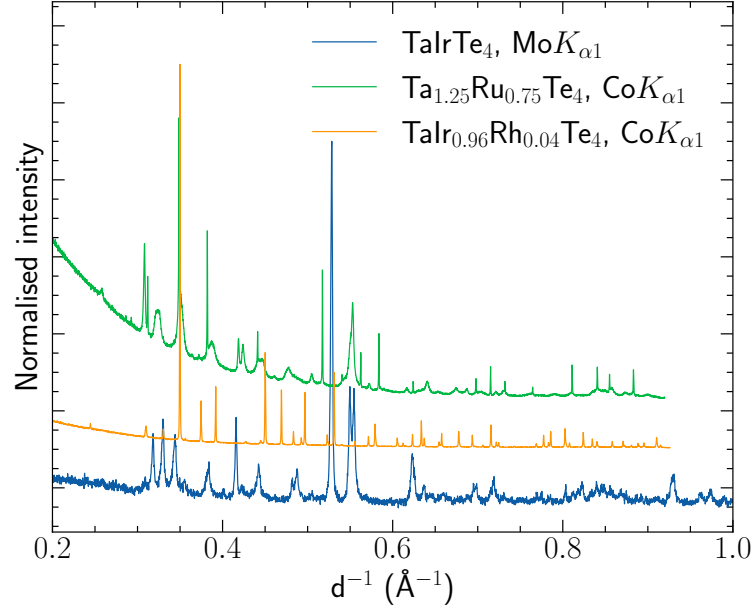


FIG. 10. Powder x-ray diffraction patterns for  $\text{TaIrTe}_4$ ,  $\text{Ta}_{1.26(2)}\text{Ru}_{0.75(2)}\text{Te}_{4.000(8)}$  and  $\text{TaIr}_{1-x}\text{Rh}_x\text{Te}_4$  ( $x = 0.04$ ).

TABLE I. comparison of nominal and composition measured in EDX for  $\text{TaIr}_{1-x}\text{Rh}_x\text{Te}_4$  crystals

Ir:Rh, nominal	EDX composition
$\text{Ir}_{0.9}\text{Rh}_{0.1}$	$\text{TaIr}_{0.96}\text{Rh}_{0.04}\text{Te}_4$
$\text{Ir}_{0.7}\text{Rh}_{0.3}$	$\text{TaIr}_{0.82}\text{Rh}_{0.14}\text{Te}_4$
$\text{Ir}_{0.3}\text{Rh}_{0.7}$	$\text{TaIr}_{0.22}\text{Rh}_{0.78}\text{Te}_4$
$\text{Ir}_{0.2}\text{Rh}_{0.8}$	$\text{TaIr}_{0.08}\text{Rh}_{0.92}\text{Te}_4$

TABLE II. Refined atomic coordinates for TaRhTe<sub>4</sub>

No	atom label		x	y	z	Occ.	Site	Sym.
1	Ta	Ta1	0.00000	0.05580	-0.19200	1.000	2a	m..
2	Ta	Ta2	0.00000	0.26530	0.29100	1.000	2a	m..
3	Rh	Rh1	0.00000	0.52760	-0.19800	1.000	2a	m..
4	Rh	Rh2	0.00000	0.75430	0.33100	1.000	2a	m..
5	Te	Te1	0.00000	0.05945	0.19049	1.000	2a	m..
6	Te	Te2	0.00000	0.19454	0.62601	1.000	2a	m..
7	Te	Te3	0.00000	0.34483	-0.09190	1.000	2a	m..
8	Te	Te4	0.00000	0.40783	0.44478	1.000	2a	m..
9	Te	Te5	0.00000	0.57274	0.19981	1.000	2a	m..
10	Te	Te6	0.00000	0.67725	0.65759	1.000	2a	m..
11	Te	Te7	0.00000	0.85038	-0.07740	1.000	2a	m..
12	Te	Te8	0.00000	0.90438	0.46746	1.000	2a	m..